RSC Advances

ROYAL SOCIETY OF CHEMISTRY

www.rsc.org/advances

Three-dimensionally ordered macroporous SiO_2-supported transition metal oxide catalysts: Facile synthesis and high catalytic activity for diesel soot combustion

Xuehua Yu[1,2], *Zhen Zhao*[1]*, *Yuechang Wei*[1]*, *Jian Liu*[1], *Jianmei Li*[1], *Aijun Duan*[1], *Guiyuan Jiang*[1]

1. State Key Laboratory of Heavy Oil Processing and Beijing Key Laboratory of Oil and Gas Pollution Control, China University of Petroleum, 18# Fuxue Road, Chang Ping, Beijing 102249, China

2. Institute of Catalysis for Energy and Environment, Shenyang Normal University, Shenyang 110034, China

Author information

Corresponding authors:

* Tel: 86-10-89731586; Fax: 86-10-69724721; E-mail zhenzhao@cup.edu.cn; weiyc@cup.edu.cn

Abstract

Three-dimensionally ordered macroporous (3DOM) SiO_2 was synthesized by colloidal crystal template (CCT) method, and 3DOM SiO_2-supported transition metal oxides catalysts were prepared by facile incipient-wetness impregnation method. The as-prepared catalysts show well-defined three-dimensionally ordered macroporous structures. The transition metal oxides formed different sizes of nanoparticles and loaded on the 3DOM SiO_2. The as-prepared catalysts show high catalytic activities for soot combustion. Among the studied catalysts, 3DOM MnO_x/SiO_2 catalyst (molar ratio of Mn to Si is 1:4) shows the highest catalytic activity among the studied catalysts, e.g. T_{10}, T_{50} and T_{90} are 297, 355 and 393 ^oC, respectively, and S^m_{CO2} is 95.5%. The catalytic performance of 3DOM SiO_2-supported transition metal oxide catalysts are mainly controlled by three factors: the macroporous effects of 3DOM structure, the redox properties of transition metal oxides and the sizes of transition metal oxides NPs. 3DOM SiO_2-supported transition metal oxide catalysts are promising for practical applications in soot combustion owing to high activity and low cost.

Keywords: Three-dimensionally ordered macroporous (3DOM) catalysts; SiO_2; transition metal oxide; catalytic activity; soot combustion

1 Introduction

Nowadays, toxicological and epidemiological studies indicate that soot particles of diesel exhaust are threatening the environment and people's health.[1] A great number of illness, which include irritation of the eyes, throat vomiting, light-headedness, headache, heartburn, bronchitis, lung cancer or even premature death and so on, have been triggered by soot particles.[2] In addition, soot particles are also a main source of urban atmospheric particulate matters (PM2.5).[3] A lot of previous works demonstrated that the exhaust of diesel engine is one of the largest contributors to soot particles in the most large and medium-sized cities. Therefore, elimination of diesel engine exhaust (especially for soot particles) is urgent for development of society and economy.[4] Indeed, great efforts have been made to reduce the soot particles to meet the stringent environmental regulations and protect human health.[5] Researches indicate that the after-treatment of diesel exhaust is one of the most perspective techniques, and the catalyst is one of important controlling factors for soot elimination.[6,7] Therefore, the development of novel catalyst is one of the most important tasks for elimination of soot particles.

A number of catalysts have been studied for soot combustion at low temperatures, including noble metals[8], perovskite-type oxides[9], CeO_2-based oxides[10,11], etc. Since it is a gas-solid-solid reaction for catalytic soot combustion, it is affected by two factors, the contact efficiency between soot and catalyst, and the intrinsic activity of catalyst. Because traditional catalysts show smaller pore sizes (<10 nm) than soot particles

(>20 nm), soot particles are difficult to enter the inner pores of these catalysts.[12] Recently, three-dimensionally ordered macroporous materials with uniform pore size (>50 nm) and well-defined structure have been applied in the field of heterogeneous catalysis.[13-15] Due to ordered macroporous structures, soot particles could easily enter their inner pores, and thus they flexibly access the active sites. A series of 3DOM metal mixed oxides, including $La_{1-x}K_xCoO_3$[16] and $Ce_{1-x}Zr_xO_2$[17] and so on, have been prepared in our group, and they all show better catalytic performances than corresponding nanoparticle catalysts for soot oxidation. The intrinsic activity of catalyst is another factor for enhancing catalytic activity after resolving the contact efficiency. To further improve the intrinsic activity of catalysts, our group have prepared a series of 3DOM oxides-supported Au or/and Pt catalysts.[18-22] Those catalysts all exhibit super high catalytic activities for soot combustion. However, due to the limited resources, noble metal catalysts are very expensive than metal oxide catalysts, which restricts the extensive application of noble metal catalysts.

In the past decades, low-cost catalysts, including single metal oxides, mixed metal oxides, perovskites, spinels, alkali earth metals and alkali metals, etc. showed high catalytic activity for soot combustion.[23-26] As always, nano-catalysts have been used in the field of catalysis and they show excellent catalytic activities in many reactions especially for oxidation reactions.[27-29] Therefore, the nano-catalysts are also expected to exhibit high catalytic activities for soot combustion.[31,32] However, design and preparation of low cost catalysts to combine nano-effect and macroporous effect are promising for increasing of catalytic activity for soot combustion and practical

application. Researchers have demonstrated that transition metal oxides with changing valence states display excellent redox properties when they are applied in the oxidation reactions.[33-36] Based on the above reasons, transition metal oxides nanoparticles (NPs) supported on 3DOM SiO_2, are expected to enhance catalytic performance for soot combustion by making the best of nano-effect and macroporous effect in 3DOM SiO_2-supported transition metal oxide catalysts.

In this paper, 3DOM SiO_2 support was synthesized by colloidal crystal template (CCT) method. 3DOM SiO_2-supported transition metal oxide catalysts were prepared by incipient wetness impregnation method. The physical and chemical properties of as-prepared catalysts were characterized by means of X-ray diffraction (XRD), scanning electron microscopy (SEM), transmission electron microscopy (TEM), temperature-programmed reduction with H_2 (H_2-TPR) measurements, UV-Vis diffuse reflectance spectra (DRS) and X-ray photoelectron spectra (XPS) etc. The catalytic performances of as-prepared catalysts were evaluated for soot combustion, and the effects of different transition metal oxide on the catalytic activities for soot combustion were investigated.

2 Experimental

2.1 Catalysts preparation

2.1.1 Synthesis of highly well-defined PMMA microspheres

The synthesis of monodispersed PMMA (polymethyl methacrylate) microsphere and the assembly template are similar to that described previously[22]. Detailed procedures are described in supporting information.

2.1.2 Synthesis of 3DOM SiO_2

3DOM SiO_2 was synthesized by colloidal crystal template (CCT) method with PMMA arrays as template and using tetraethyl orthosilicate (TEOS) as precursors. In a typical procedure, 4.6 g TEOS was dissolved into the mixture of water (2.5 mL), alcohol (5 mL) and HCl aqueous solution (2mol/L, 2.5 mL). After that, the hydrolyzation was proceeded in a water bath at 35 ^{o}C for 4 h. Then, 3g PMMA arrays were added into the above solution for impregnation. After complete impregnation, the PMMA arrays with the precursor solution were separated by vacuum filter and dried at 30 ^{o}C for 24 h. The dried samples were calcined to remove the CCT in a tube furnace with an air flow (80 mL min^{-1}). The temperature-rising rate was 1 ^{o}C min^{-1} from room temperature to 600 ^{o}C, and the temperature of calcination at 600 ^{o}C was kept for 4 h, and then 3DOM SiO_2 supports were obtained.

2.1.3 Synthesis of 3DOM SiO_2-supported transition metal oxide catalysts

3DOM SiO_2-supported transition metal oxide catalysts were prepared by incipient-wetness impregnation method. In a typical procedure, a certain amount of transition metal nitrates (50 wt% $Mn(NO_3)_2$ aqueous solution, $Fe(NO_3)_3 \cdot 9H_2O$, $Co(NO_3)_2 \cdot 6H_2O$, $Ni(NO_3)_2 \cdot 6H_2O$, $Cu(NO_3)_2 \cdot 3H_2O$) were dissolved into deionized water, and then the above aqueous solution was added into 3DOM SiO_2. After that, the impregnated sample was dealt with ultrasonic for 10 min and dried at 80 ^{o}C for 24 h. Then, the sample was calcined at 550 ^{o}C for 4 h in tube furnace and 3DOM SiO_2-supported transition metal oxide catalysts were obtained. The stoichiometric ratios of raw materials for 3DOM SiO_2-supported transition metal oxide catalysts are

listed in the Table 1. In addition, different loading amounts of manganese nitrate on 3DOM SiO_2 were also prepared and the corresponding dosages of raw materials are also listed in the Table 1.

2.2 Physical and chemical characterization

XRD patterns were measured on a powder X-ray diffractometer (Bruker D8 Advance) using CuKa (k=0.15406 nm) radiation with a Nickel filter operating with voltage and current of 40 kV and 40 mA in the 2θ range of 10-90^o at a scanning step of 0.02^o. The patterns were compared with JCPDS reference data for phase identification. The surface morphology of the catalyst was observed by field emission scanning electron microscopy (FESEM) on a Quanta 200F instruments using accelerating voltages of 5 kV. SEM samples were dusted on conducting resin and coated with 10 nm Au prior to measurement. The TEM images were obtained using a JEOL JEM-2100 transmission electron microscope. A typical TEM sample was prepared by adding several droplets of a nanoparticles/ethanol mixture onto a carbon-coated copper grid. Nitrogen adsorption/desorption isotherms at -196 ^{o}C were recorded using a Micromeritics TriStar II 3020 porosimetry analyzer. The samples were degassed at 300 ^{o}C for 4 h prior to the measurements.

H_2-TPR was performed using a Quantachrome Autosorb-iQ, USA. A sample of 100 mg was loaded into a U-shaped quartz reactor and pre-treated in Ar at 300 ^{o}C for 1 h. After cooling to room temperature, the flow gas was switched to 10-vol% H_2/Ar, and the catalyst was heated to 900 ^{o}C at a rate of 10 ^{o}C min^{-1}. The flow rate of 10-vol% H_2/Ar is 50 mL min^{-1}. The consumption of hydrogen was recorded by thermal

conductivity detector (TCD). Calibration of the instrument was carried out with CuO of known amount. X-ray photoelectron spectra (XPS) were recorded on a Perkin-Elmer PHI-1600 ESCA spectrometer using Mg Kα X-ray source. The binding energies were calibrated using C1s peak of contaminant carbon (BE = 284.6 eV) as an internal standard.

2.3 Activity measurements

The catalytic performances of all catalysts were evaluated with a temperature-programmed oxidation reaction (TPO) on a fixed-bed tubular quartz reactor (Φ= 8 mm), and each TPO run from 150 to 650 ^{o}C at a 2 ^{o}C min^{-1} rate. The model soot was Printex-U particulates (diameter 25 nm, purchased from Degussa). The catalyst (100 mg) and soot (10 mg) were mixed at a weight ratio of 10:1 with a spatula in order to reproduce the loose contact mode. Reactant gases (50 mL min^{-1}) contain 10% O_2 and 0.2% NO balanced with Ar. The outlet gas compositions were analyzed with an on-line gas chromatograph (GC, Sp-3420, Beijing) by using FID detectors. Before entering the FID detector, CO and CO_2 were fully converted to CH_4 by a convertor with Ni catalyst at 380 ^{o}C. The catalytic activity was evaluated by the values of T_{10}, T_{50} and T_{90}, which were defined as the temperatures at 10%, 50% and 90% of soot conversion, respectively. The selectivity to CO_2 formation (S_{CO_2}) was defined as that the CO_2 outlet concentration (C_{CO_2}) divided by the sum of the CO_2 and CO outlet concentration, i.e., $S_{CO_2}= C_{CO_2}/(C_{CO} + C_{CO_2})$. $S^{m}_{CO_2}$ was denoted as S_{CO_2} at the maximum temperature corresponding to the soot-burnt rate was the highest. In all TPO experiments, the reaction was not finished until the soot was completely burnt

off.

3 Results and discussion

3.1 Catalyst characterization

3.1.1 The results of XRD

XRD patterns of 3DOM SiO_2-supported transition metal catalysts are shown in Figure 1. As shown in Figures 1a-g, different transition metal catalysts exhibit various diffraction peaks. For the pure SiO_2 (Figure 1a), a broad peak at 2θ of 23.5^o can be observed, which is typical peak of amorphous silica.[37] An overview of the XRD patterns of as-prepared 3DOM transition metal catalysts in Figures 1b-f indicates that transition metal oxides formed after the process of calcination. The detailed explanations about 3DOM SiO_2-supported transition metal catalysts are shown in the Supplementary Information. In addition, from the Figures 1b-f, it can be seen that the peak of amorphous silica disappeared when transition metal oxides were supported on the surface of 3DOM SiO_2. The XRD patterns of 3DOM SiO_2-supported MnO_x catalysts with different MnO_x loading amounts are shown in Figures 1g-j. With the increasing of MnO_x loading amount, the intensity of diffraction peaks of amorphous SiO_2 becomes weaken and some feature peaks of manganese oxide appear and their intensities enhance. As shown in Figures 1i-j, the diffraction peaks of SiO_2 almost disappear when the loading amount of MnO_x is over a certain value (molar ratio of Mn to Si is over 1:4). It is attributed to MnO_x coated on the surface of 3DOM SiO_2.

3.1.2 The results of SEM

Figure 2 shows the SEM images of 3DOM SiO_2-supported transition metal

catalysts with loading of different transition metals. The SEM images show that the macropores with average diameter of ca. 310±20 nm are interconnected through open windows, ca. 90-140 nm in diameter, and the wall thicknesses are ca. 30-50 nm[17]. As shown in the Figures 2a-f, it can be seen that the macropores have uniform pore sizes, windows and wall thicknesses, and those macropores are highly periodically arrayed and interconnected through small windows. These SEM images clearly demonstrate that all 3DOM samples have long range ordered macroporous structure. As shown in the inserted SEM images, some dark dots in macropores were visible clearly. The SEM images suggest that the process of supporting transition metal oxides on 3DOM SiO_2 has no influence on 3DOM structure.

Figure 3 shows the SEM images of 3DOM SiO_2-supported MnO_x catalysts with different MnO_x loading amounts. From the Figure 3 and Figure 2b, it can be seen that 3DOM structue is clearly observed when the ratio of Mn to Si is lower than 1:4 (Figures 3a,b and Figure 2b), while 3DOM structue has a little destruction when the molar ratio of Mn to Si is over 1:4 (Figures 3c,d). The reason for the result may be that the excess MnO_x agglomerated and formed big particles. 3DOM structure of SiO_2 is affectted by the big particles. From the all SEM images with different MnO_x loading amounts, it can be concluded that 3DOM structue can be maintain when MnO_x loading amount is lower than a certain constant (molar ratio of Mn to Si is 1:4).

3.1.3 The results of TEM

TEM images of 3DOM SiO_2-supported transition metal catalysts with loadings of different transition metals are shown in Figure 4. From the Figure 4a, it can be seen

that 3DOM SiO_2 with over-lapped pores can be clearly observed by TEM image. No granular or spherical SiO_2 are observed on the surface of 3DOM SiO_2. Combined with XRD result of SiO_2 (Figure 1a), it indicates that the framework of 3DOM SiO_2 was accumulated by amorphous SiO_2. As shown in Figures 3b, c, the surface of 3DOM SiO_2 is successfully decorated with well-dispersed MnO_x and Fe_2O_3 nanoparticles (NPs), and no larger agglomerated particles is observed. The MnO_x NPs with particle size of 10-30 nm and Fe_2O_3 NPs with particle size of 4-13 nm are adhered on the walls of 3DOM SiO_2. The average MnO_x and Fe_2O_3 NPs sizes are estimated to be 23.5±3.6 and 8.6±2.4 nm for 3DOM MnO_x/SiO_2 and Fe_2O_3/SiO_2 catalysts, respectively. And the particle size of Co_3O_4 NPs on 3DOM Co_3O_4/SiO_2, which the average value is about 60 nm in Figure 4d, is much bigger than 3DOM MnO_x/SiO_2 catalysts. The TEM image (Figure 4e) of NiO/SiO_2 catalyst shows that NiO NPs are supported on the surface of 3DOM SiO_2, while the particle size of NiO NPs is located in the range of 20-50 nm. This large particle size is disadvantageous to the catalytic activity of catalyst. TEM image of CuO/SiO_2 (Figure 4e) shows that the part of dark place is bulk CuO, indicating that bulk CuO formed in the process of calcination. The SEM (Figure 2) and TEM (Figure 4) images of 3DOM SiO_2-supported transition metal catalysts suggest that 3DOM structure of SiO_2 well maintains and the transition metal oxides exhibit different particle sizes with different transition metal elements.

Figure 5 shows the TEM images of 3DOM SiO_2-supported MnO_x catalysts with different MnO_x loading amounts. From Figures 5a,b and Figure 4b, it can be seen that the surface of 3DOM SiO_2 is successfully decorated with well-dispersed MnO_x NPs

and no larger agglomerated particles is observed when molar ratio of Mn to Si is less than 1:4. The MnO_x NPs with particle size of 10-30 nm are adhered on the walls of 3DOM SiO_2. However, the particle size of MnO_x NPs increases with increasing of MnO_x loading amount. The particle sizes of MnO_x particles are about 50 nm and 150 nm for MnO_x/SiO_2 when molar ratios of Mn to Si are 1:3 and 1:2. It is attributed to that the concentration of impregnation liquid ($Mn(NO_3)_2$ aqueous solution) become higher and higher with the increasing of molar ratio of Mn to Si. As shown in the Figure 5d, most of MnO_x particles are supported on outside surface of 3DOM SiO_2 and no small MnO_x particles can be observed on the inner surface of 3DOM SiO_2. This agglomeration of active component of MnO_x/SiO_2 catalyst may lead to low catalytic activity for soot combustion when molar ratio of Mn to Si is 1:2.

3.1.4 The results of BET

Nitrogen adsorption-desorption isotherms for 3DOM SiO_2-supported transition metal catalysts were tested and the results are shown in Figure 6. The as-prepared catalysts exhibit similar adsorption-desorption isotherm shapes. However, their hysteretic loops are different when different transition metals support on 3DOM SiO_2. As shown in Figure 6a and b, 3DOM SiO_2 and 3DOM SiO_2-supported MnO_x catalyst show obvious hysteretic loops, while the others exhibit small hysteretic loops. The values of surface area, total pore volume and pore size are listed in the Table 2. 3DOM SiO_2 shows the highest surface area among the as-prepared 3DOM catalysts and its value is 270.1 m^2/g. The scraggly surface of 3DOM SiO_2 may contribute to enhancing the surface area owing to no nanoparticles on the surface. In addition,

3DOM SiO_2 shows the lowest pore size among the as-prepared catalysts. The surface area obviously decreased when transition metals supported on 3DOM SiO_2. As shown in the Table 2, the order of surface area value for as-prepared catalysts is as follows: Fe_2O_3/SiO_2 > MnO_x/SiO_2 > NiO/SiO_2 > Co_3O_4/SiO_2 > CuO/SiO_2. Combined with the TEM images in Figure 4, the reason for this order can be explained by the size of transition metals nanoparticles. In other words, small nanoparticles will contribute to enhancing the surface area owing to high surface area of small NPs. The total pore volume and pore size of as-prepared catalysts are different with the different transition metals. 3DOM SiO_2 shows the highest total pore volume and pore size among the as-prepared catalysts. From the results of SEM and TEM, it can be seen that the pore sizes of as-prepared catalysts are more than 300 nm. However, as shown in the Table 2, the pore sizes of as-prepared catalysts are less than 10 nm. The reason for this phenomenon is that the value of pore size (based on BET results) is calculated by BJH desorption average pore diameter. This calculation method does not contain the macropores. Therefore, the pore sizes (based on BET results) of as-prepared catalysts are less than 10 nm.

3.1.5 The results of UV-Vis diffuse reflectance spectra

The UV-Vis DRS of 3DOM SiO_2-supported transition metal catalysts were obtained at room temperature in the range of 200-800 nm. From the Figure 7a, it can be seen that pure 3DOM SiO_2 has almost no absorption in the ultraviolet and visible region.[38] As shown in Figure 7b and 8g-j, the relative UV-Vis absorption spectrum of MnO_x/SiO_2 indicated the multivalent oxidation states of Mn. Combined with the XPS

results, the peaks in the range of 200-350 nm range could be reasonably assigned to $O^{2-} \rightarrow Mn^{3+}$ charge transfer transitions in the MnO_x. While the broad peak at 450 nm was ascribed to the d-d electron transitions of Mn^{3+} and Mn^{4+}.[39] From Figure 7c, it can be seen that the absorption of Fe_2O_3/SiO_2 was rapidly faded when wavelengths is longer than 560 nm. The broad absorption from 300 to 560 nm corresponds to the $^6A_1+^6A_1 \rightarrow ^4T_1(^4G)+^4T_1(^4G)$ excitation of an Fe^{3+}-Fe^{3+} pair. The absorption at 200 -300 nm is ascribed to the ligand to metal charge transfer transitions and partly contributed from the Fe^{3+} ligand field transitions $^6A_1 \rightarrow ^4T_1(^4P)$.[40] As shown in Figure 7d, the UV-Vis spectra exhibited three different absorbance edges at 200-300, 400-600 and 700-800 nm for Co_3O_4/SiO_2. The bands ($\lambda < 500$ nm) can be assigned to the $O^{2-} \rightarrow Co^{2+}$ charge transfer process, while the band ($\lambda > 700$ nm) was due to the $O^{2-} \rightarrow Co^{3+}$ charge transfer.[41] The UV-Vis DRS of NiO/SiO_2 is reported in Figure 7e. The spectrum of NiO/SiO_2 shows a strong absorption in the UV region, similar to an absorption plateau with two predominant components at 240 and 300 nm, in agreement with literature data.[42] The absorption spectrum of CuO/SiO_2 (Figure 7f) revealed several absorption bands. The band appeared in the 220-360 nm spectral range can be assigned to the charge transfer transition of the ligand O^{2+} to isolated metal center Cu^{2+} and the d-d transition in CuO particles. The signal appeared between 650-800 nm could be ascribed to the $2E_g \rightarrow 2T_{2g}$ spin-allowed transitions of Cu^{2+} in the distorted octahedral symmetry.[43]

3.1.6 The results of H_2-TPR

It is well known that soot catalytic combustion is a complicated gas-solid

(soot)-solid (catalyst) three-phase reaction. The intrinsic redox properties of catalysts play a key role in the combustion of soot. In this work, the redox properties of catalysts were characterized by H_2-TPR measurements and the results are shown in the Figure 8. As shown in Figures 8a-f, the peak positions and types of 3DOM SiO_2-supported transition metal catalysts vary with different kinds of transition metal. From the H_2-TPR profile of 3DOM SiO_2 (Figure 8a), it can be seen that no reduction peak is observed, indicating that 3DOM SiO_2 exhibits none redox property. Figure 8b shows the H_2-TPR profile of MnO_x/SiO_2, two main reduction peaks with peak temperatures at 320 and 416 ^oC can be observed. Assuming that MnO is the final state in the reduction of Mn species.[44] The peak at 230 -350 ^oC could be assigned to the reduction of MnO_2/Mn_2O_3 to Mn_3O_4, and the peak at 350-500 ^oC may be assigned to the reduction of Mn_3O_4 to MnO. The results indicate that substantial amount of Mn^{4+} and Mn^{3+} in MnO_x/SiO_2 catalyst can be reduced to Mn^{2+} below 500 °C, which is consistent with the previous reports.[45] Figure 8c depicts the H_2-TPR profile of Fe_2O_3/SiO_2, two main peaks, whose peak temperatures are located at 351 and 523 ^oC, are characteristics of two reduction steps. The first peak may be assigned to the reduction of Fe_2O_3 to Fe_3O_4, whereas the second may be attributed to the transition from Fe_3O_4 to FeO. Besides the above two main peaks, a weak reduction peak located at 600 ^oC can be assigned to the reduction of Fe_3O_4 to to FeO in the inner Fe_2O_3 nanoparticles. Due to small particle sizes and high dispersion of Fe_2O_3 NPs, the reduction temperatures are lower than previously reported works. Previous studies found that the reduction behavior of Co_3O_4 is highly dependent on the dispersion state

of cobalt. Large particles of Co_3O_4 were usually reduced to metallic cobalt by a single step while nanoparticles often went through a two-step process.[46] As shown in the Figure 8d, two reduction peaks, of which a minor reduction peak at 329 ^oC and main reduction peak at 376 ^oC, are observed for Co_3O_4/SiO_2 catalyst owing to Co_3O_4 NPs with particle size of 60 nm. The two overlapped reduction peaks are corresponded to the reduction of $Co_3O_4 \rightarrow CoO \rightarrow Co$.[47] Figure 8e shows the H_2-TPR profiles of NiO/SiO_2 catalyst. Two overlapped reduction peaks with two peak maxima at 350 ^oC and 415 ^oC are obtained, which are consistent with the reduction of two types of Ni^{2+}/Ni^{3+} species to metallic nickel.[48,49] The H_2-TPR profile of CuO/SiO_2 is shown in Figure 8f. The minor shoulder reduction peak at 222 ^oC is assigned to reduction of dispersed copper oxide, while the main reduction peak at 281 ^oC is corresponded to reduction of CuO.[42,50] The different reduction peaks of 3DOM SiO_2-supported transition metal catalysts indicate that those catalysts may exhibit various catalytic activities for soot combustion. Figures 8g-j display the H_2-TPR profiles of 3DOM MnO_x/SiO_2 catalysts with different MnO_x loading amounts. Two main reduction peaks can be obtained in Figures 8g-j. The peak temperatures increase with the increasing of MnO_x loadings. The first and second reduction peak temperatures increase from 300 to 336 ^oC and from 417 to 456 ^oC, respectively, for the sample with molar ratio of Mn to Si from 1:16 to 1:2. The possible reason for this result is that particle size of MnO_x increases with the increasing of MnO_x loadings (Figure 5). In addition, the intensity of H_2 consumption peak also increases with the increasing of MnO_x loading amounts. Based on the above results of H_2-TPR, transition metal

oxides show high redox property owing to different chemical valence states of transition metal. The catalytic activity is possibly associated with the changing capacity of varied oxidation states and with ‘‘oxygen mobility’’ in the oxide lattice. This property may contribute to the enhancement of catalytic activity for soot combustion.

3.1.7 The results of XPS

Figure 9Aa displays the XPS spectrum of Mn 2p for 3DOM MnO_x/SiO_2 catalysts. The Mn 2p spectrum is significantly broadened and showed some asymmetry towards both Mn $2p_{3/2}$ and Mn $2p_{1/2}$ peaks. The binding energies of the XPS Mn $2p_{3/2}$ peak are found to be in the range 639.0-645.0 eV. Two kinds of Mn species including Mn^{3+} (ca. 641.5eV), and Mn^{4+} (644.5 eV) are presented on the surface of as-prepared catalysts. Meanwhile, the Mn $2p_{1/2}$ peak also shows two kinds of Mn species at BEs range of 650-657 eV.[22] From Figure 9Ab, it can be seen that the Fe 2p spectrum of Fe_2O_3/SiO_2 is split into $2p_{3/2}$ (710.6 eV) and $2p_{1/2}$ (724.1 eV) doublets due to the spin-orbit coupling. According to the previous reports, the remarkable features of Fe_2O_3/SiO_2 in XPS spectrum is a characteristic of Fe^{3+} in Fe_2O_3.[51] In addition, there is a satellite peak at 718.9 eV beside the main peak of Fe $2p_{3/2}$ at 710.9 eV, which is also an evidence for Fe^{3+} in Fe_2O_3. The XPS result of Fe_2O_3/SiO_2 is also in good agreement with the XRD result. As shown in Figure 9Ac, two spin orbit components of Co (Co $2p_{3/2}$ at 779.6 eV and Co $2p_{1/2}$ at 795.1 eV) and two weak satellites at higher energy (786-790 and 800-805 eV) for both Co peaks are obtained. The BE difference between Co $2p_{1/2}$ and Co $2p_{3/2}$ peaks is 15.5 eV, and it is in agreement with previously

reported for Co_3O_4.[52,53] The Ni 2p XPS spectrum (Figure 9Ad) shows two characteristic double peaks of Ni $2p_{1/2}$ and Ni $2p_{3/2}$. The additional peak located at around 879.2 eV and 860.8 eV are the satellite of Ni $2p_{1/2}$ and Ni $2p_{3/2}$.[54] According to the literature, the satellite peaks of Ni $2p_{1/2}$ and Ni $2p_{3/2}$ indicate that Ni^{3+} ions or Ni^{2+}-OH species is present in NiO/SiO_2. Here, the Ni^{3+} only refers to a structure containing vacancies in the NiO but does not indicate an existence of Ni_2O_3 phase in NiO/SiO_2.[55] Figure 9Ae shows the spin-orbit split of Cu $2p_{1/2}$ and Cu $2p_{3/2}$ at 954.6 eV and 934.5 eV, respectively. The gap between Cu $2p_{1/2}$ and Cu $2p_{3/2}$ is 20.1 eV, which is similar with the standard spectrum of CuO. The existence of satellite peaks (943.7 and 962.5 eV) is an indicator of the Cu^{2+} ions, which is excluded the possibility of Cu_2O phase in CuO/SiO_2 catalyst.[56]

The corresponding O 1s XPS spectra are present in Figure 9B. Three types of O species is defined as O-I, O-II and O-III. The O-I component located at 529.5 eV are ascribed to lattice oxygen ions bonded to transition metal cations[57]. Because of different transition metals, the BEs of O-I have a small shift from 529.4 to 530.4 eV. The dominating O-II component at BEs 532.6~ 533.1 eV is obviously related to O^{2-} species in SiO_2 (Si-O-Si environments).[58] The minor O-III component located at ~535.1 eV may include contributions from Si-OH groups. As shown in Figure 9C, the values of BEs for Si 2p are changed with different transition metals. The Si 2p spectra of the catalysts (Figure 9C) are dominated by a peak centered at BEs of 103.0~103.6 eV, characteristic of Si^{4+} in SiO_2. The reason for shifted BEs is that different transition metals change the chemical environment of Si-O-Si bands. In addition, as shown in

Table S1, the surface compositions of as-prepared catalysts are different with bulk composition. The surface oxygen ratios are higher than corresponding bulk oxygen ratios, indicates that as-prepared catalysts will exhibit high catalytic activity for soot combustion.

3.2 Activity test

3.2.1 Catalytic activities for soot combustion

The catalytic activities of 3DOM SiO_2-supported transition metal catalysts for soot oxidation were evaluated and the results are listed in Table 3. To compare the catalytic activities of as-prepared catalysts, the combustion reactions of pure soot and 3DOM SiO_2 were also estimated under the same reaction conditions. For the pure soot, the T_{10}, T_{50} and T_{90} are 482, 564 and 609 ^{o}C, respectively. The 3DOM SiO_2 also shows somewhat catalytic activity for soot combustion, and the T_{10}, T_{50} and T_{90} are 354, 503 and 550 ^{o}C, respectively. This result indicates that the 3DOM structure of SiO_2 can enhance the contact area between soot and reaction gas when the soot and SiO_2 are met. All the 3DOM SiO_2-supported transition metal catalysts show high catalytic activities for soot combustion. However, different SiO_2-supported transition metal catalysts exhibit various catalytic activities. Compared the values of ΔT_{10}, ΔT_{50} and ΔT_{90} of 3DOM SiO_2-supported transition metal catalysts in the Table 3, 3DOM MnO_x/SiO_2 catalyst shows the highest catalytic activity for soot combustion, the ΔT_{10}, ΔT_{50} and ΔT_{90} of are 173, 202 and 212 ^{o}C, respectively. These results suggest that MnO_x is optimal choice for soot combustion in those transition metal oxides. In addition, 3DOM SiO_2-supported transition metal catalysts show much higher CO_2

selectivity for soot combustion than that of pure soot combustion, and the values are all surpassed 90%. The CO_2 selectivity value of 3DOM MnO_x/SiO_2 catalyst is as high as 95.5%. These experimental results suggest that 3DOM MnO_x/SiO_2 catalyst is promising catalysts for soot combustion. In order to more clearly describe the results of Table 3, the CO_2 concentration profiles for soot combustion over 3DOM SiO_2-supported transition metal catalysts were listed in the Figure S1. From Figure S1A, it can be seen that the CO_2 concentration profiles are corresponding to the results of Table 3. 3DOM SiO_2-supported transition metal catalysts with various transition metal exhibit different catalytic activities. As shown in Figure S1B, the changing tendency of catalytic activities is very similar to the result of Table 3.

As shown in Table 3, the catalytic activities of 3DOM SiO_2-supported transition metal catalysts with varied transition metal oxides follow the order: MnO_x/SiO_2 > Co_3O_4/SiO_2 > Fe_2O_3/SiO_2 > CuO/SiO_2 > NiO/SiO_2. Combined the results of TEM (Figures 4) and H_2-TPR (Figures 8b-f), the different particle sizes, redox properties of transition metal oxides and valence state of transition metal element can explain the varied catalytic activities of 3DOM SiO_2-supported transition metal catalysts. The H_2-TPR results of as-prepared catalysts indicate that CuO/SiO_2 may give the highest catalytic activity for soot combustion due to the lowest reduction temperature among those catalysts. However, TEM image of CuO/SiO_2 exhibits that bulk CuO is formed, which is disadvantage for soot combustion owing to low contact effect between soot and catalyst. In addition, previous reports have proved that CuO does not have the capacity of adsorbing oxygen.[59,60] Therefore, CuO/SiO_2 catalyst presents very low

activity for particulate matter oxidation. TEM image of Fe_2O_3/SiO_2 displays that Fe_2O_3 NPs with particle size of 4-13 nm are highly dispersed on the wall of 3DOM SiO_2. This result suggests that soot and Fe_2O_3/SiO_2 catalyst may be well contacted with soot. And 3DOM Fe_2O_3/SiO_2 catalyst is presumed to show high catalytic activity. In fact, it exhibits lower catalytic activity than MnO_x/SiO_2 and Co_3O_4/SiO_2 catalysts. The reason for this phenomenon is that 3DOM Fe_2O_3/SiO_2 catalyst shows the highest reduction temperature among those catalysts. Based on the above two reasons, 3DOM Fe_2O_3/SiO_2 catalyst exhibits low catalytic activity for soot combustion. Except for particle sizes and redox properties, the valence states also exhibit significant influence on catalytic activity. As shown in the results of XPS, there are two kinds of valence states for MnO_x/SiO_2 while only one kind of valence state for other catalysts. The catalyst with different valence states will enhance the capability of oxygen activation. In the process of soot combustion, the redox reaction of Mn^{3+}/Mn^{4+} in the MnO_x/SiO_2 is in favor of forming oxygen vacancies on the surface of catalysts, and then the active oxygen can be easily generated on the vacancies sites. Therefore, MnO_x/SiO_2 shows the highest catalytic activity for soot combustion.

In order to demonstrate the impaction of NO, we also tested the catalytic performance of MnO_x/SiO_2 under different reaction conditions, and the results are listed in the following Table S2. Compared with pure soot, the MnO_x/SiO_2 catalyst shows super catalytic activity for soot combustion when they reacted under the same reaction conditions (2000 ppm NO, 10% O_2). This result indicates that our prepared catalysts exhibit high catalytic performance for soot combustion when NO is

participated in soot combustion. As shown in Table S2, the catalytic activities of MnO_x/SiO_2 catalyst decrease with the decreasing of concentrations of NO. However, the catalytic activity of MnO_x/SiO_2 is also much higher that pure soot even no NO is participated in the reaction. Those above results obviously demonstrate that the reaction pathways of soot combustion can be divided into two parts: One is that active oxygen species directly oxidize soot particles; the other one is that NO_2 acts as intermediate to catalyze soot oxidation.

The MnO_x loading amount has a significant effect on the catalytic performance of 3DOM MnO_x/SiO_2. The catalytic activity first increases with the increasing MnO_x loadings (molar ratio of Mn to Si is 1:4), and then it decreases with further increasing of MnO_x loading amount. The H_2-TPR results of 3DOM MnO_x/SiO_2 with different MnO_x loadings indicate that high MnO_x loadings give large amount of H_2 consumption, which can increase the catalytic activity for soot combustion. However, there is a suitable MnO_x loading amount for the catalyst to get high catalytic activity. Combined the TEM results in Figure 5, the particle sizes of MnO_x NPs increase from 20 nm to 150 nm with increasing MnO_x loadings (molar ratio of Mn to Si increased from 1:16 to 1:2). The free spread of soot particles in 3DOM structure would be blocked by big MnO_x NPs (150 nm) owing to 90-140 nm of interconnected windows in 3DOM MnO_x/SiO_2 (Figure 3). According to the above reasons, 3DOM MnO_x/SiO_2 catalyst (molar ratio of Mn to Si is 1:4) exhibits the highest catalytic activity.

3.2.2 Stability of 3DOM MnO_x/SiO_2 catalyst

In order to demonstrate the stability of as-prepared catalysts, the catalytic activity

and CO_2 selectivity of 3DOM MnO_x/SiO_2 catalyst in five cycles were examined and the results are shown in Figure 10. The catalytic activity and CO_2 selectivity of 3DOM MnO_x/SiO_2 catalyst keep constant after reaction for five times under the condition of loose contact between catalysts and soot particles. The temperature values of T_{10}, T_{50} and T_{90} are 297±5, 355±6 and 393±5°C, respectively. Meanwhile, the CO_2 selectivity value is higher than 95% even after five-cycle reaction. The stability test results indicate that 3DOM MnO_x/SiO_2 catalyst has good stability for soot combustion.

3.2.3 The effect of 3DOM structure in as-prepared catalysts on soot combustion

As a gas-solid-solid reaction, soot combustion is affected by two factors, including redox property of catalyst and contact efficiency between soot and catalyst. Besides the high redox property, the contact between soot and catalysts also plays an important role in improving the catalytic activity. Because loose contact between soot particles and catalysts is a main way of contact in the process of after-treatment for diesel engine exhaust, it is extremely important to study and design the active catalysts, which can improve the contact efficiency between the catalysts and soot particles under loose contact conditions. In this work, 3DOM SiO_2-supported transition metal catalysts with uniform macropores are designed and synthesized to enhance the contact efficiency. As shown in Figure 2 and Figure 4, the average diameter of ordered macroporous is about 310 nm and diameter of transition metal oxides NPs is lower than 50 nm (except for Co_3O_4/SiO_2 and CuO/SiO_2). Therefore,

soot particles could easily across those macropores and contact with transition metal oxides NPs (supported on the wall of 3DOM SiO_2). To demonstrate the macroporous effect, the soot and 3DOM MnO_x/SiO_2 catalyst was studied under the same conditions of TPO reaction to demonstrate the contact efficiency. In this confirmatory experiment, the reaction temperature of soot and 3DOM catalyst was programmed to 290 ^oC, which means the soot was not ignited. From the TEM image of Figure 11a, it can be seen that soot particles entered into the macropores of 3DOM MnO_x/SiO_2 catalyst. In addition, the outside soot particles could enter the inner pores of 3DOM catalyst with the help of the reaction gas flow (O_2, NO and Ar) during the reaction process owing to a gas-solid-solid reaction for soot combustion. More importantly, the rising reaction temperature may be contributed to accelerating the movement of soot particles. Under the influence of gas flow and rising temperature, the outside soot particles can easily enter into the 3DOM structure and contact the inner active sites of 3DOM catalyst. As shown in the Figure 11b, the macropores of 3DOM MnO_x/SiO_2 are well contacted with soot particles, indicating that 3DOM structure is a desirable feature for diesel soot combustion. As shown in the HRTEM images (Figure 11c), the soot and MnO_x NPs are well contact with each other in the inner of 3DOM structure. Therefore, the number of available active sites of catalysts can be maximized through macroporous effect, especially for inner active sites of catalysts. More active sites would result in higher catalytic activity. TEM results directly demonstrate that soot particles can easily enter the interior of 3DOM catalysts with the help of the airflow in the reaction process under the loose contact conditions, and have less resistance to go through the

catalyst structure. In fact, our group has synthesized a series of 3DOM materials and they show higher catalytic activities than the corresponding particle materials. Therefore, it is significantly important to study and design 3DOM structure for soot combustion.

4. Conclusions

In summary, 3DOM SiO_2 support was successfully synthesized by CCT method. Different transition metal oxides NPs with varied sizes are supported on the skeleton of 3DOM SiO_2 by simple incipient-wetness impregnation method. All 3DOM SiO_2-supported transition metal catalysts show high periodical arrayed macropores and interconnected small windows. 3DOM SiO_2-supported catalysts with different transition metal oxides NPs exhibit different catalytic activities for soot combustion. Compared with pure soot, 3DOM MnO_x/SiO_2 catalyst with molar ratio of Mn:Si is 1:4 shows the highest catalytic activity among the as-prepared catalysts, which T_{10}, T_{50} and T_{90} are 297, 355 and 393 ^oC, respectively. The CO_2 selectivity of as-prepared catalysts is also higher than 93%. The macroporous effects of 3DOM structure, redox properties of transition metal oxides and sizes of transition metal oxide NPs significantly affect the catalytic activity for soot combustion simultaneously. The as-prepared catalysts are promising for practical applications in the catalytic oxidation of diesel soot particles owing to high activity and low cost.

Acknowledgements

This work was financially supported by NSFC (Nos. 21177160, 21303263 and

21477164), Beijing Nova Program (NO. Z141109001814072), Specialized Research Fund for the Doctoral Program of High Education of China (NO. 20130007120011) and the Science Foundation of China University of Petroleum-Beijing (No. 2462013YJRC13 and 2462013BJRC003).

References

1 T. W. Hesterberg, C. A. Lapin and W. B. Bunn, *Environ. Sci. Technol.,* 2008, **42**, 6437-6445.

2 R. Prasad and V. R. Bella, *Bull. Chem. Rea. Eng. Catal.* 2010, **5**, 69-86.

3 M. V. Twigg, *Appl. Catal., B,* 2007, **70**, 2-15.

4 M. R. Heal, P. Kumar and R. M. Harrison, *Chem. Soc. Rev.* 2012, **41**, 6606-6630.

5 D. R. Treea and K. I. Svensson, *Prog. Energy Combust. Sci.,* 2007, **33**, 272-309.

6 J. P. A. Neeft, M. Makkee and J. A. Moulijn, *Appl. Catal., B,* 1996, **8**, 57-78.

7 A. Bueno-López, *Appl. Catal., B,* 2014,146, 1-11.

8 X. D. Wu, S. Liu and D. Weng, *Catal. Sci. Technol.*, 2011,**1**, 644-651.

9 Y. Teraoka, K. Nakano, W. F. Shangguan and S. Kagawa, *Catal. Today,* 1996, **27**, 107-113.

10 X. D. Wu, F. Lin, H.B. Xu and D. Weng, *Appl. Catal., B,* 2010, **96**, 101-109.

11 Q. Q. Yang, F. N. Gu, Y. F. Tang, H. Zhang, Q. Liu, Z. Y. Zhong and F. B. Su, RSC Adv., 2015,**5**, 26815-26822

12 J. A. Sullivan, P. Dulgheru, I. Atribak, A. Bueno-López and A. García-García, *Appl. Catal., B,* 2011, **108-109**, 134-139.

13 H. Arandiyan, H. X. Dai, J. G. Deng, Y. X. Liu, B. Y. Bai, Y. Wang, X. W. Li, S. H. Xie and J. H. Li, *J. Catal.,* 2013, **307**, 327-339.

14 M. Sadakane, K. Sasaki, H. Kunioku, B. Ohtani, W. Ueda and R. Abe, *Chem. Commun.*, 2008, **48**, 6552-6554.

15 A. Stein, B. E. Wilson and S. G. Rudisill, *Chem. Soc. Rev.*, 2013, **42**, 2763-2803.

16 J. F. Xu, J. Liu, Z. Zhao, C. M. Xu, J.X. Zheng, A. J. Duan, G. Y. Jiang and *J.*

Catal., 2011, **282**, 1-12.

17 G. Z. Zhang, Z. Zhao, J.F. Xu, J.X. Zheng, J. Liu, G.Y. Jiang, A.J. Duan and H. He, *Appl. Catal., B,* 2011, 107, 302-315.

18 Y. C. Wei, J. Liu, Z. Zhao, Y.S. Chen, C.M. Xu, A.J. Duan, G. Y. Jiang and H. He, *Angew. Chem. Int. Ed.,* 2011, **50**, 2326-2329.

19 Y. C. Wei, J. Liu, Z. Zhao, A. J. Duan, G. Y. Jiang, C.M. Xu, J. S. Gao and H. He, *Energy Environ. Sci.*, 2011, **4**, 2959-2970.

20 Y. C. Wei, J. Liu, Z. Zhao, C. M. Xu, G. Y. Jiang and A. J. Duan, *Small,* 2013, **9**, 3957-3963.

21 Y. C. Wei, Z. Zhao, J. Liu, S.T. Liu, C.M. Xu, A.J. Duan and G.Y. Jiang, *J. Catal.,* 2014, **317**, 62-74.

22 X. H. Yu, J. M. Li, Y. C. Wei, Z. Zhao, J. Liu, B. F. Jin, A. J. Duan and G. Y. Jiang, *Ind. Eng. Chem. Res.,* 2014, **53**, 9653-9664.

23 Z. L. Zhang, Y. X. Zhang, Q. Y. Su, Z. P. Wang, Q. Li and X.Y. Gao, *Environ. Sci. Technol.,* 2010, **44**, 8254-8258.

24 X.D. Wu, S. Liu, D. Weng and F. Lin, *Catal. Commun.*, 2011,**12**, 345-348.

25 S. Quiles-Díaz, J. Giménez-Mañogila and Avelina García-García, *RSC Adv.*, 2015,**5**, 17018-17029.

26 H. Zhang, F. Gu, Q. Liu, J. J. Gao, L. H. Jia, T. Y. Zhu, Y. F. Chen, Z. Y. Zhong and F. B. Su, *RSC Adv.*, 2014,**4**, 14879-14889

27 D. Fino and V. Specchia, *Powder Technol.,* 2008, **180**, 64-73.

28 X. H. Yu, J. H. He, D.H. Wang, Y. C. Hu, H. Tian and Z. C. He, *J. Phys. Chem. C* 2012, **112**, 851-860.

29 Y. X. Liu, H. X. Dai, J. G. Deng, X. W. Li, Y. Wang, H. Arandiyan, S. H. Xie, H. G.Yang and G. S. Guo, *J. Catal.,* 2013, **305**, 146-153.

30 S. Liu, X. D. Wu, D. Weng, M. Li and R. Ran. *ACS Catal.,* 2015, **5**, 909-919.

31 P. Legutko, T. Jakubek, W. Kaspera, P. Stelmachowski, Z. Sojka and A. Kotarba, *Catal. Commun.,* 2014, **43**, 34-37.

32 E. Aneggi, N.J. Divins, C.de Leitenburg, J. Llorca and A. Trovarelli, *J.Catal.,* 2014, **312**, 191-194.

33 P. Yang, S. H. Yang, Z. N. Shi, Z. H. Meng and R. X. Zhou, *Appl. Catal., B* 2015, **162**, 227-235.

34 Q. Shen, M. F. Wu, H. Wang, C. He, Z. P. Hao, W. Wei and Y. H. Sun, *Catal. Sci. Technol.*, 2015, **5**, 1941-1952

35 J. Ballester, A. M. Caminade, J. P. Majoral, M. Taillefer and A. Oualib, *Catal. Commun.*, 2014, **47**, 58-62.

36 J. L. Ren, Y. F. Yu, F. F. Dai, M. Meng, J. Zhang, L.R. Zheng and T. D. Hu, *Nanoscale,* 2013,**5**, 12144-12149

37 R. M. Rioux, H. Song, J. D. Hoefelmeyer, P. Yang and G. A. Somerjai, *J. Phys. Chem. B,* 2005, **109**, 2192-2202.

38 J. L. Lu, K. M. Kosuda, R. P. Van Duyne and P. C. Stair, *J. Phys. Chem. C*, 2009, **113**, 12412-12418.

39 Y. L. Nie, C. Hu, L. Yang and J. C. Hu, *Sep. Purif. Technol.*, 2013, **117**, 41-45.

40 M. Mohammadikish, *Ceram. Int.*, 2014, **40**, 1351-1358.

41 S. Farhadi and J. Safabakhsh, *J. Alloys Compd.*, 2012, **515**, 180-185.

42 G. Garbarino, I. Valsamakis, P. Riani and G. Busca, *Catal. Commun*., 2014, **51**, 37-41

43 S. Morpurgo, M. L. Jacono and P. Porta, *J. Mater. Chem.*, 1994, **4**, 197-205.

44 M. Sun, L. Yu, F. Ye, G. Q. Diao, Q. Yu, Z. F. Hao, Y. Y. Zheng and L. X. Yuan, *Chem. Eng. J.,* 2013, **220**, 320-327.

45 G. D. Yadav and R. K. Mewada, *Chem. Eng. J.,* 2013, **221**, 500-511.

46 W. Q. Song, A. S. Poyraz, Y. T. Meng, Z. Ren, S.Y. Chen and S. L. Suib, *Chem. Mater.,* 2014, **26**, 4629-4639.

47 Y. Lou, L. Wang, , Z. Y. Zhao, Y. H. Zhang, Z. G. Zhang, G. Z. Lu, Y. Guo and Y. L. Guo, *Appl. Catal., B,* 2014, **146**, 43-49.

48 B. Solsona, P. Concepción, S. Hernández, B. Demicol and J. M. L. Nieto, *Catal. Today,* 2012, **180**, 51-58.

49 T. Takeguchi, S. Furukawa and M. Inoue, *J. Catal.,* 2001, **202**, 14-24.

50 S. Bennici, A. Gervasini, N. Ravasio and F. Zaccheria, *J. Phys. Chem. B,* 2003, **107**, 5168-5176.

51 P. F. Xie, L.F. Chen, Z. Ma, C.Y. Huang, Z. W. Huang, Y. H. Yue, W. M. Hua, Y. Tang and Z. Gao, *Microporous Mesoporous Mater.,* 2014, **200**, 52-60.

52 Z. L. Chen, S. H. Chen, Y.H. Li, X. H. Si, J. Huang, S. Massey and G. L. Chen. *Mater. Res. Bull.*, 2014, **57**, 170-176.

53 G. L. Chen, X. L. Si, J. S. Yu, H. Y. Bai and X. H. Zhang, *Appl. Surf. Sci.,* 2015, **330**, 191-199.

54 F. D. Qu, Y. F. Wang, J. Liu, S. P. Wen, Y. Chen and S. P. Ruan, *Mater. Lett.,* 2014, 132, 167-170.

55 L. Cao, D. X. Wang and R. Wang, *Mater. Lett.,* 2014, **132**, 357-360,.

56 K. Mageshwari, D. Nataraj, T. Pal, R. Sathyamoorthy and J. Park, *J. Alloys Compd.* 2015, **625**, 362-370.

57 R. R. Hu, C. F. Yan, L. Y. Xie, Y. Cheng and D. Z. Wang, *Int. J. Hydrogen Energy,* 2011, **36**, 64-71.

58 S. P. Chenakin, G. Melaet, R. Szukiewicz and N. Kruse, *J. Catal.* 2014, **312**, 1-11.

59 G. Corro, S. Cebada, U. Pal, J. L. G. Fierro and J. Alvarado, *Appl. Catal., B,* 2015, **165**, 555-565.

60 F. E. López-Suárez, A. Bueno-López and M. J. Illán-Gómez. *Appl. Catal., B,* 2008, **84**, 651-658.

Captions for Tables

Table 1 Expression ways of nominal ratio for the preparation of 3DOM SiO_2-supported transition metal oxide catalysts

Table 2 Physicochemical properties of as-prepared catalysts

Table 3 Catalytic activities of 3DOM SiO_2-supported transition metal catalysts for soot combustion

Table 1 Expression ways of nominal ratio for the preparation of 3DOM SiO_2-supported transition metal oxide catalysts

Catalysts	Kinds of Nitrates	[b]M:Si	$M(NO_3)_x$/g	3DOM SiO_2/g
MnO_x/SiO_2	[a]$Mn(NO_3)_2$	1:4	0.7516	0.5
Fe_2O_3/SiO_2	$Fe(NO_3)_3 \cdot 9H_2O$	1:4	0.6112	0.5
Co_3O_4/SiO_2	$Co(NO_3)_2 \cdot 6H_2O$	1:4	0.8484	0.5
NiO/SiO_2	$Ni(NO_3)_2 \cdot 6H_2O$	1:4	0.6106	0.5
CuO/SiO_2	$Cu(NO_3)_2 \cdot 3H_2O$	1:4	0.5074	0.5
MnO_x/SiO_2-1	$Mn(NO_3)_2$	1:16	0.1879	0.5
MnO_x/SiO_2-2	$Mn(NO_3)_2$	1:8	0.3758	0.5
MnO_x/SiO_2-4	$Mn(NO_3)_2$	1:3	1.1274	0.5
MnO_x/SiO_2-5	$Mn(NO_3)_2$	1:2	1.5032	0.5

a: 50 wt% $Mn(NO_3)_2$ aqueous solution

b: Molar ratio of transition metal elements to SiO_2, M means transition metal elements

Table 2 Physicochemical properties of as-prepared catalysts

Catalysts	Surface area (m^2/g)[a]	Total pore volume (cm^3/g)[b]	Pore size (nm)[c]
SiO_2	270.1	0.231	8.2
MnO_x/SiO_2	180.5	0.208	7.6
Fe_2O_3/SiO_2	215.4	0.135	7.8
Co_3O_4/SiO_2	145.7	0.117	6.9
NiO/SiO_2	156.7	0.129	6.8
CuO/SiO_2	136.5	0.099	6.5

a: Calculated by BET method; b: Calculated by BJH desorption cumulative volume of pores between 1.7 nm and 300 nm diameter; c: Calculated by BJH desorption average pore diameter

Table 3 Catalytic activities of 3DOM SiO_2-supported transition metal catalysts for soot combustion

Catalysts	T_{10} /°C	T_{50} /°C	T_{90} /°C	Sco_2^m/%	ΔT_{10}	ΔT_{50}	ΔT_{90}
Pure soot	482	564	609	71.6	--	--	--
3DOM SiO_2	354	503	550	78.1	128	61	59
MnO_x/SiO_2	297	355	393	95.5	185	209	216
Fe_2O_3/SiO_2	316	420	480	93.8	166	144	129
Co_3O_4/SiO_2	309	362	397	96.9	173	202	212
NiO/SiO_2	348	449	496	96.4	134	115	113
CuO/SiO_2	325	410	452	96.6	157	154	157
MnO_x/SiO_2-1	306	382	427	93.1	176	182	182
MnO_x/SiO_2-2	304	377	416	94.5	178	187	193
MnO_x/SiO_2-4	297	358	397	94.6	185	206	212
MnO_x/SiO_2-5	303	361	398	95.6	179	203	211

ΔT_{10}: The difference value of T_{10} between pure soot and catalysts

ΔT_{50}: The difference value of T_{50} between pure soot and catalysts

ΔT_{90}: The difference value of T_{50} between pure soot and catalysts

Captions for Figures

Fig. 1 X-ray diffraction patterns of 3DOM SiO_2-supported transition metal catalysts. a: SiO_2, b: MnO_x/SiO_2("▲" represents for Mn_2O_3 and "△" represents for Mn_3O_4), c: Fe_2O_3/SiO_2("☆" represents for Fe_2O_3), d: Co_3O_4/SiO_2("★"represents for Co_3O_4), e: NiO/SiO_2("■"represents for NiO), f: CuO/SiO_2("□"represents for CuO); molar ratio of Mn to Si: g: 1:16; h: i:8; c: 1:3; j: 1:2.

Fig. 2 SEM images of 3DOM SiO_2-supported transition metal catalysts. a: SiO_2; b: MnO_x/SiO_2; c: Fe_2O_3/SiO_2; d: Co_3O_4/SiO_2; e: NiO/SiO_2; f: CuO/SiO_2.

Fig. 3 SEM images of 3DOM SiO_2-supported MnO_x catalysts. Molar ratio of Mn to Si: a: 1:16; b: 1:8; c: 1:3; d: 1:2

Fig. 4 TEM images of 3DOM SiO_2-supported transition metal catalysts. a: SiO_2; b: MnO_x/SiO_2; c: Fe_2O_3/SiO_2; d: Co_3O_4/SiO_2; e: NiO/SiO_2; f: CuO/SiO_2.

Fig. 5 TEM images of 3DOM SiO_2-supported MnO_x catalysts. Molar ratio of Mn to Si: a: 1:16; b: 1:8; c: 1:3; d: 1:2

Fig. 6 Nitrogen adsorption-desorption isotherms of 3DOM SiO_2-supported transition metal catalysts. a: SiO_2; b: MnO_x/SiO_2; c: Fe_2O_3/SiO_2; d: Co_3O_4/SiO_2; e: NiO/SiO_2; f: CuO/SiO_2.

Fig. 7 UV-Vis DRS of 3DOM SiO_2-supported transition metal catalysts. a: SiO_2, b: MnO_x/SiO_2, c: Fe_2O_3/SiO_2, d: Co_3O_4/SiO_2, e: NiO/SiO_2, f: CuO/SiO_2; molar ratio of Mn to Si: g: 1:16; h: i:8; c: 1:3; j: 1:2

Fig. 8 H_2-TPR profiles of 3DOM SiO_2-supported transition metal catalysts. a: SiO_2, b: MnO_x/SiO_2, c: Fe_2O_3/SiO_2, d: Co_3O_4/SiO_2, e: NiO/SiO_2, f: CuO/SiO_2; molar ratio of Mn to Si: g: 1:16; h: i:8; c: 1:3; j: 1:2

Fig. 9 XPS spectra of 3DOM SiO_2-supported transition metal catalysts. a: MnO_x/SiO_2; b: Fe_2O_3/SiO_2; c: Co_3O_4/SiO_2; d: NiO/SiO_2; e: CuO/SiO_2.

Fig. 10 Stability tested results of 3DOM MnO_x/SiO_2 catalyst for soot combustion (molar ratio of Mn to Si is 1:4,)

Fig. 11 TEM (a,b) and HRTEM (c) images of 3DOM MnO_x/SiO_2 and soot particles

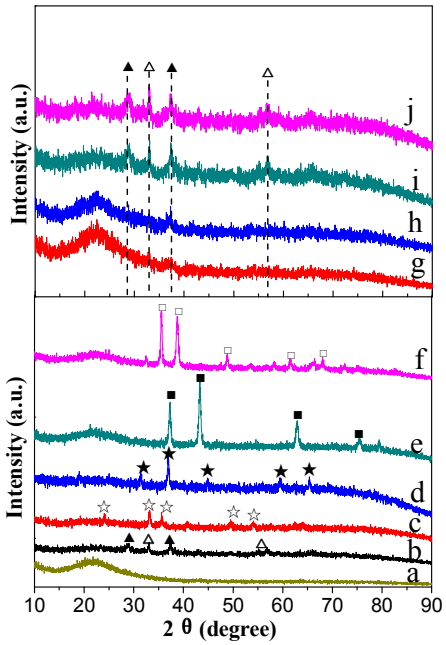

Fig. 1 X-ray diffraction patterns of 3DOM SiO_2-supported transition metal catalysts. a: SiO_2, b: MnO_x/SiO_2("▲" represents for Mn_2O_3 and "△" represents for Mn_3O_4), c: Fe_2O_3/SiO_2("☆" represents for Fe_2O_3), d: Co_3O_4/SiO_2("★"represents for Co_3O_4), e: NiO/SiO_2("■"represents for NiO), f: CuO/SiO_2("□"represents for CuO); molar ratio of Mn to Si: g: 1:16; h: i:8; c: 1:3; j: 1:2.

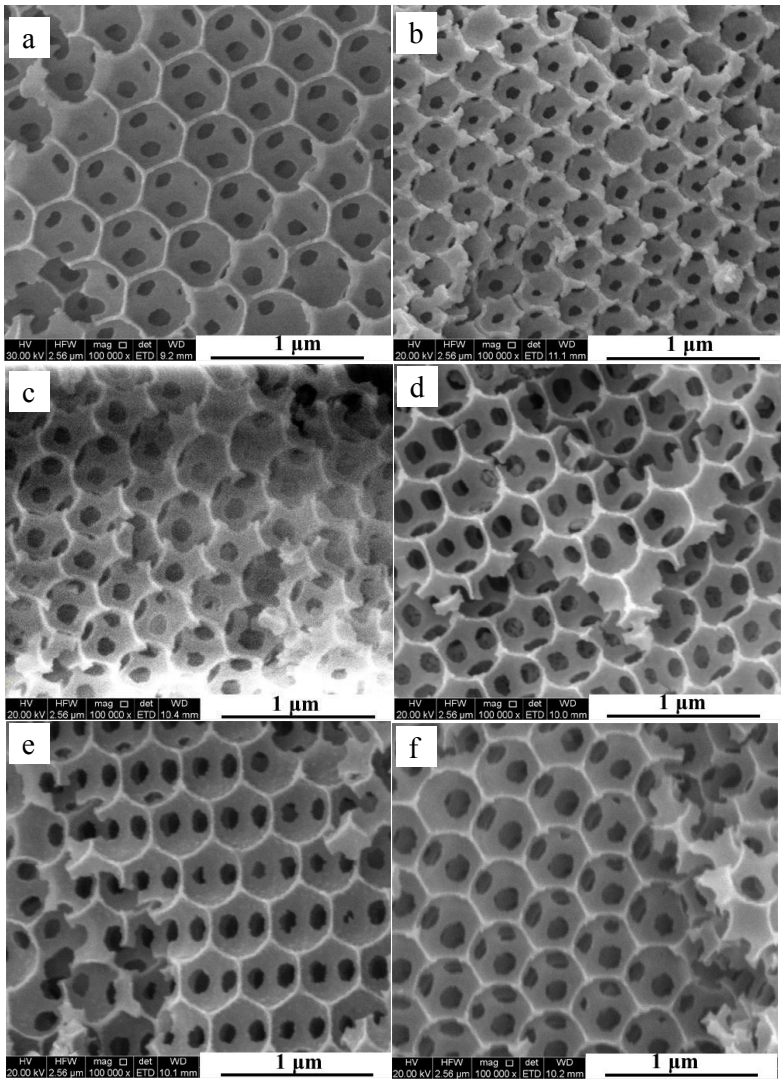

Fig. 2 SEM images of 3DOM SiO_2-supported transition metal catalysts
a: SiO_2; b: MnO_x/SiO_2; c: Fe_2O_3/SiO_2; d: Co_3O_4/SiO_2; e: NiO/SiO_2; f: CuO/SiO_2.

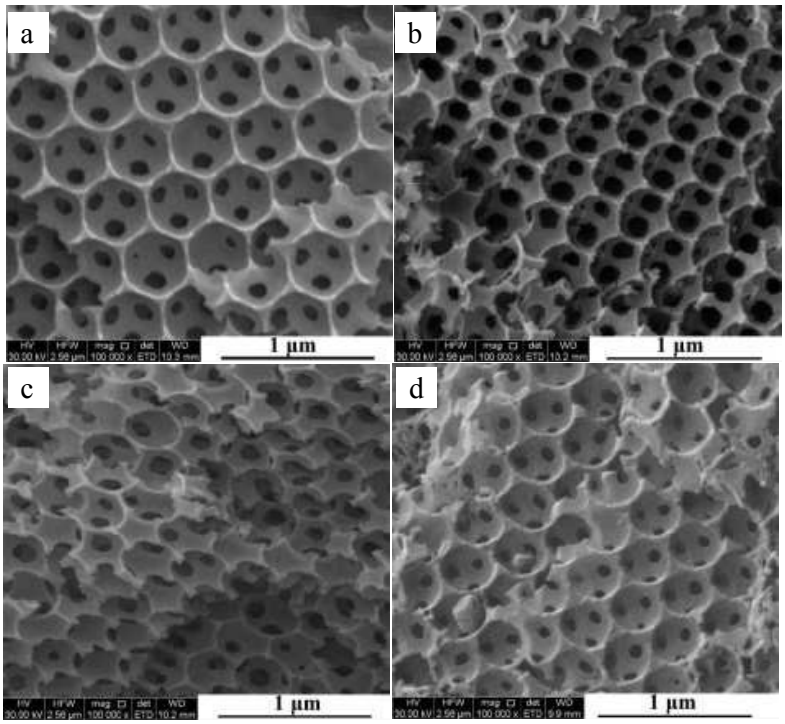

Fig. 3 SEM images of 3DOM SiO_2-supported MnO_x catalysts. Molar ratio of Mn to Si: a: 1:16; b: 1:8; c: 1:3; d: 1:2

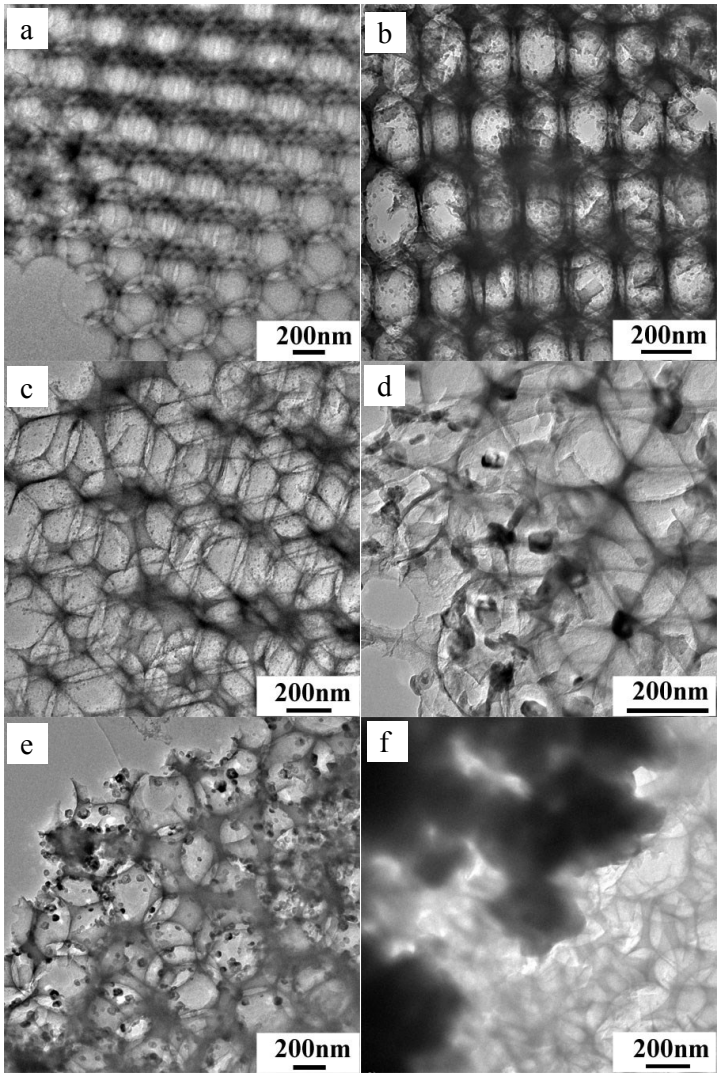

Fig. 4 TEM images of 3DOM SiO_2-supported transition metal catalysts. a: SiO_2; b: MnO_x/SiO_2; c: Fe_2O_3/SiO_2; d: Co_3O_4/SiO_2; e: NiO/SiO_2; f: CuO/SiO_2.

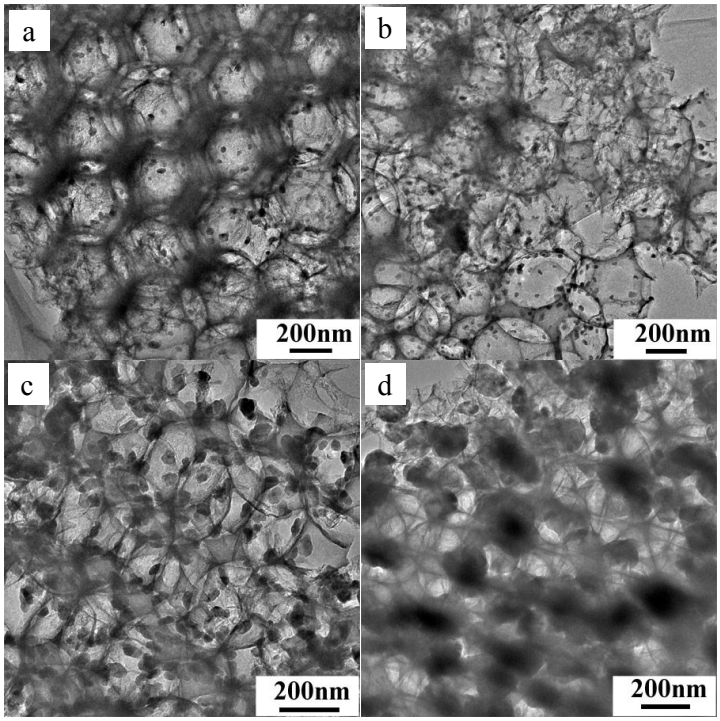

Fig. 5 TEM images of 3DOM SiO_2-supported MnO_x catalysts. Molar ratio of Mn to Si: a: 1:16; b: 1:8; c: 1:3; d: 1:2

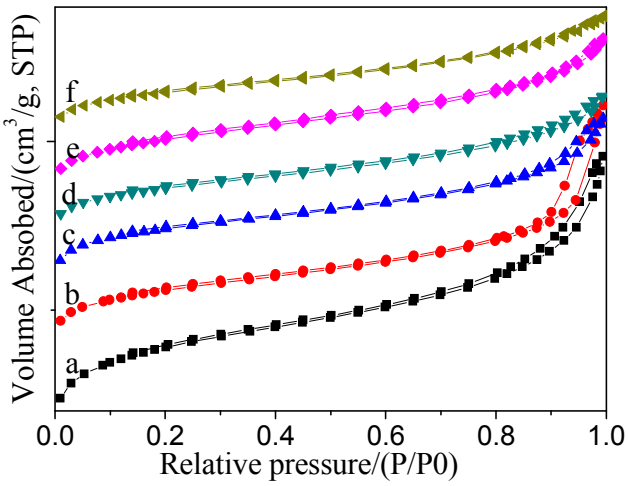

Fig.6 Nitrogen adsorption-desorption isotherms of 3DOM SiO_2-supported transition metal catalysts

a: SiO_2; b: MnO_x/SiO_2; c: Fe_2O_3/SiO_2; d: Co_3O_4/SiO_2; e: NiO/SiO_2; f: CuO/SiO_2.

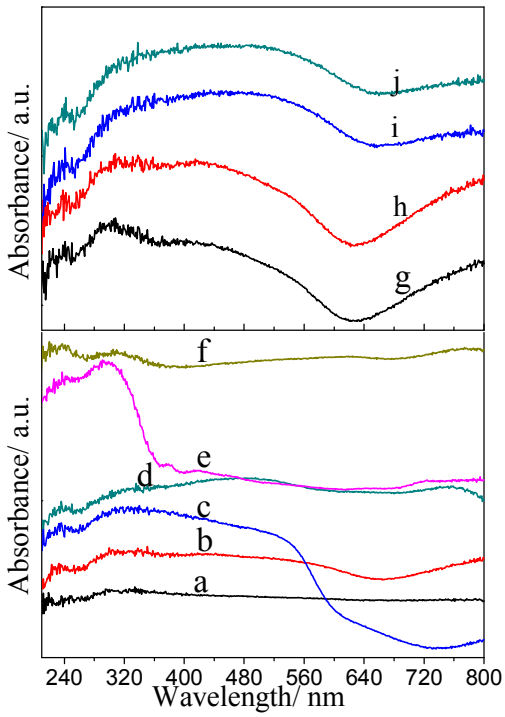

Fig. 7 UV-Vis DRS of 3DOM SiO_2-supported transition metal catalysts. a: SiO_2, b: MnO_x/SiO_2, c: Fe_2O_3/SiO_2, d: Co_3O_4/SiO_2, e: NiO/SiO_2, f: CuO/SiO_2; molar ratio of Mn to Si: g: 1:16; h: i:8; c: 1:3; j: 1:2

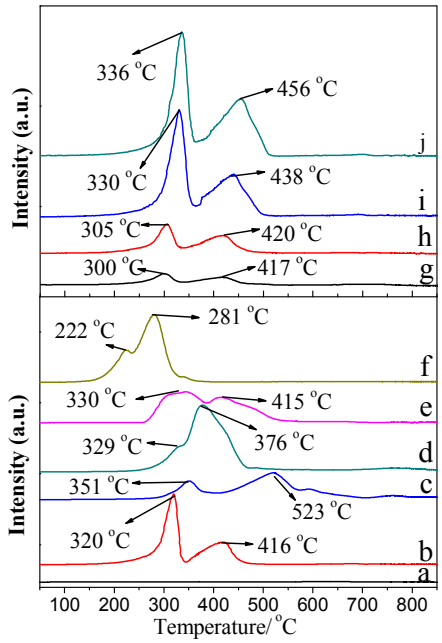

Fig. 8 H_2-TPR profiles of 3DOM SiO_2-supported transition metal catalysts. a: SiO_2, b: MnO_x/SiO_2, c: Fe_2O_3/SiO_2, d: Co_3O_4/SiO_2, e: NiO/SiO_2, f: CuO/SiO_2; molar ratio of Mn to Si: g: 1:16; h: 1:8; i: 1:3; j: 1:2

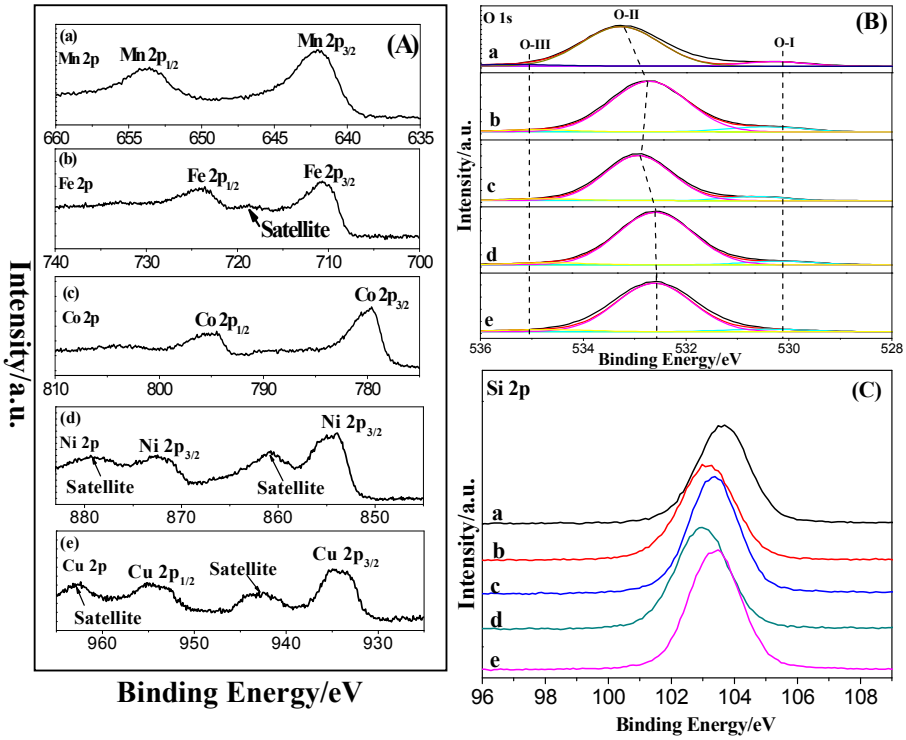

Fig. 9 XPS spectra of 3DOM SiO_2-supported transition metal catalysts. a: MnO_x/SiO_2; b: Fe_2O_3/SiO_2; c: Co_3O_4/SiO_2; d: NiO/SiO_2; e: CuO/SiO_2.

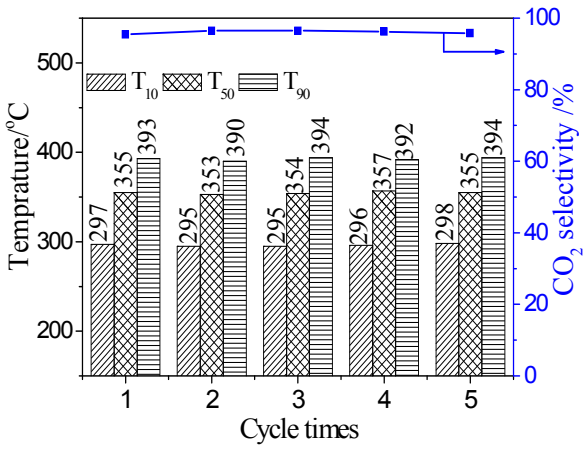

Fig. 10 Stability tested results of 3DOM MnO_x/SiO_2 catalyst for soot combustion (molar ratio of Mn to Si is 1:4)

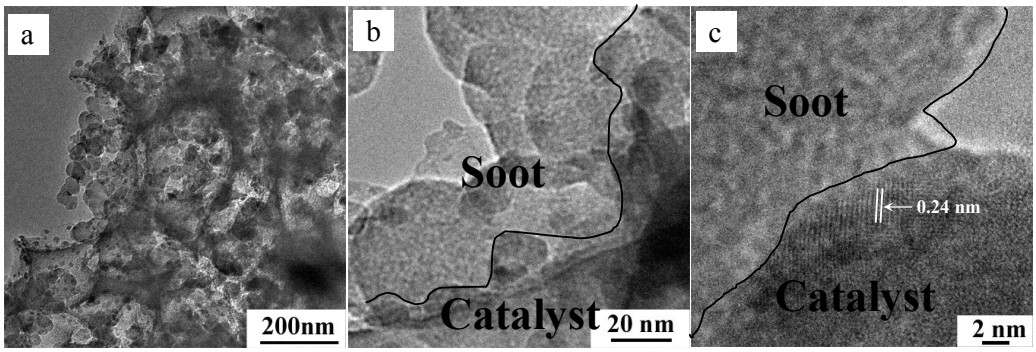

Fig. 11 TEM (a,b) and HRTEM (c) images of 3DOM MnO_x/SiO_2 and soot particles